Published in final edited form as:
Neuroimage. 2013 December ; 83: . doi:10.1016/j.neuroimage.2013.07.055.

Evaluation of slice accelerations using multiband echo planar imaging at 3 Tesla

Junqian Xu[1,‡], **Steen Moeller**[1,‡], **Edward J. Auerbach**[1], **John Strupp**[1], **Stephen M. Smith**[2], **David A. Feinberg**[3,4], **Essa Yacoub**[1], and **Kâmil Uğurbil**[1]

[1]Center for Magnetic Resonance Research, Department of Radiology, University of Minnesota, USA

[2]FMRIB Centre, Oxford University, UK

[3]Advanced MRI Technologies, Sebastopol, CA, USA

[4]Helen Wills Institute for Neuroscience, University of California Berkeley, CA, USA

Abstract

We evaluate residual aliasing among simultaneously excited and acquired slices in slice accelerated multiband (MB) echo planar imaging (EPI). No in-plane accelerations were used in order to maximize and evaluate achievable slice acceleration factors at 3 Tesla. We propose a novel leakage (*L*-) factor to quantify the effects of signal leakage between simultaneously acquired slices. With a standard 32-channel receiver coil at 3 Tesla, we demonstrate that slice acceleration factors of up to eight (MB = 8) with blipped controlled aliasing in parallel imaging (CAIPI), in the absence of in-plane accelerations, can be used routinely with acceptable image quality and integrity for whole brain imaging. Spectral analyses of single-shot fMRI time series demonstrate that temporal fluctuations due to both neuronal and physiological sources were distinguishable and comparable up to slice-acceleration factors of nine (MB = 9). The increased temporal efficiency could be employed to achieve, within a given acquisition period, higher spatial resolution, increased fMRI statistical power, multiple TEs, faster sampling of temporal events in a resting state fMRI time series, increased sampling of q-space in diffusion imaging, or more quiet time during a scan.

Keywords

lipped CAIPI; leakage (*L*-) factor; *g*-factor; residual aliasing; spectral analysis; single-shot fMRI time series

Corresponding author: Junqian Xu, Center for Magnetic Resonance Research (CMRR), Department of Radiology, University of Minnesota Medical School, 2021 6th St. SE, Minneapolis, MN 55455, jxu@umn.edu or junqian.xu@mssm.edu.
‡The first two authors contributed equally.
Dr. Xu is now affiliated with Icahn School of Medicine at Mount Sinai.

1. INTRODUCTION

The recent availability of high and ultrahigh magnetic fields has enabled acquisitions of functional magnetic resonance imaging (fMRI) data with increasingly higher spatial resolution and finer detail, e.g. (De Martino et al., 2011; Heidemann et al., 2012; Polimeni et al., 2010; Yacoub et al., 2008; Zimmermann et al., 2011). Acquisitions of such high-resolution data over the entire human brain in a time efficient manner, however, face severe challenges using conventional approaches. Almost all fMRI studies currently employ a multi-slice approach based on slice selective gradient recalled echo (GRE) echo planar imaging (EPI) (Mansfield, 1977) due to its wide-spread availability and the fast single-slice acquisition speed of the EPI method for spatial encoding. Over the years, the acquisition speed of EPI has significantly improved with the advent of partial Fourier sampling (Feinberg et al., 1986) and parallel imaging (Griswold et al., 2002; Pruessmann et al., 1999; Sodickson and Manning, 1997) methods, resulting in reductions in the amount of *k*-space data collected and, hence, the total echo train length in an EPI acquisition. These improvements have led to important gains in EPI image quality; however, they have not commensurately impacted the speed of whole brain coverage due to the presence of contrast preparation period in applications like fMRI or diffusion weighted imaging, which equals or exceeds the total duration of the EPI echo train. Consequently, even with EPI, whole brain coverage unavoidably requires prolonged volume acquisition times (TR), especially when the targeted volume are required to be covered in high isotropic resolutions. In turn, this limits the total number of time points and the sampling bandwidth in an fMRI time series, especially at lower field strengths where longer echo delays (i.e. TEs) are needed for optimal blood oxygenation level dependent (BOLD) contrast.

Three dimensional (3D) echo volume imaging (EVI) (Mansfield et al., 1994) uses a single contrast preparation period followed by a single 3D *k*-space encoding readout. However, EVI has limited achievable spatial resolution and potentially sub-standard image quality, due to the T_2* decay during a long echo train required to fully encode the volumetric spatial information. In addition, distortions on two of the 3D image axes and losses in signal-to-noise ratio (SNR) are present, as well as signal dropout in regions close to air filled cavities in the head, such as the temporal lobes and inferior frontal cortex. Multi-shot segmented EVI along with parallel imaging can significantly alleviate these problems (Poser et al., 2010; Posse et al., 2012; Wielopolski et al., 1995). However, to achieve this efficiently, parallel imaging is employed on the two orthogonal phase encoding dimensions, leading to considerable SNR losses. Furthermore, *k*-space segmentation can lead to degraded *k*-space coherence (Feinberg and Oshio, 1994), which is especially detrimental to functional imaging (Moeller et al., 2006). Echo shifting approaches, such as PRESTO (Golay et al., 2000; Liu et al., 1993), increase volume coverage in fMRI by efficiently utilizing the TE delay to readout a different earlier excited slice. PRESTO, however, requires additional spoiling that reduces SNR and spatial encoding and becomes constrained at higher field strengths where the shorter T_2 and T_2* curtail the usable TE for the BOLD contrast. Consequently, these approaches have not been able to supplant multi-slice GRE EPI as the dominant method employed in fMRI.

The multi-band (MB) or simultaneous multi-slice (SMS) technique was originally demonstrated with leg imaging using a spine radio frequency (RF) coil and GRE acquired with one *k*-space line at a time (Larkman et al., 2001). In the MB approach, several slices are simultaneously excited using a single RF pulse tailored for selective excitation at multiple frequencies (i.e., a multiband pulse), and subsequently unaliased following parallel imaging principles. The application of MB to EPI was first introduced by Nunes et al. (Nunes et al., 2006) in brain imaging. Motivated by the possibility of acquiring high resolution functional brain images at 7 Tesla over the entire brain (Uğurbil, 2012), we

recently first evaluated the prospect of using MB-EPI for fMRI (Moeller et al., 2010). We demonstrated a 16-fold, two-dimensional acceleration yielding significant reduction in whole brain acquisition time without substantial degradation in SNR or image quality (Moeller et al., 2010, 2008). Slice acceleration using MB technique was also recently combined with the SIR technique (Feinberg et al., 2002; Loenneker et al., 1996) for fMRI and diffusion weighted imaging (Feinberg et al., 2010; Setsompop et al., 2012), adopted for steady state free precession (SSFP, (Stäb et al., 2011)), radial (Yutzy et al., 2011), and spiral (Poser and Stenger, 2012) acquisitions, and incorporated into Hadamard encoding (Banerjee et al., 2012; Chu et al., 2012).

The ability to unalias the MB GRE slices was improved by the controlled aliasing in parallel imaging results in higher acceleration (CAIPIRINHA) method (Breuer et al., 2005). This was achieved by alternating the phase of the excitation pulses progressively for each *k*-space line in a GRE sequence, which collected a single *k*-space line after each RF pulse. The phase modulation results in a spreading of the aliasing energy and an exploitation of coil sensitivity profiles along multiple dimensions, thereby reducing *g*- factor and significantly expanding the acceleration capability of the receiver coil. Unfortunately, in EPI, only one RF excitation is used for all *k*-space lines in the entirety of *k*-space coverage; therefore, modulation of the RF pulse phase (Jesmanowicz et al., 2011) to shift simultaneously excited slices relative to each other is not possible. Instead, it was demonstrated that small slice gradient pulses ("blipped pulses") could be employed during the EPI echo train to accomplish the same result. The first demonstration of this principle utilized slice gradient blips which resulted in a linear accumulation of gradient moment to achieve aliased image shifts in the phase encoding direction (Nunes et al., 2006) with an interdependent tilting of the voxel. This limitation of the linear gradient blip strategy was overcome by the recently introduced blipped controlled aliasing in parallel imaging (blipped CAIPI) technique (Setsompop et al., 2012), a modulated gradient moment scheme of slice blips that does not result in tilted voxels. The blipped CAIPI method has also been adopted into segmented EPI (Polimeni et al., 2012) and readout-segmented EPI (Frost et al., 2012).

In the current paper, we introduce a leakage (*L*-) factor (Moeller et al., 2012) for quantitatively evaluating the performance of the MB technique, with respect to residual aliasing among simultaneously excited and acquired slices. In the absence of in-plane acceleration, we examined the feasibility of achieving up to eight simultaneously excited slices with acceptable image quality at 3 Tesla using a standard 32-channel receiver coil. The effects of neuronal and physiological signal fluctuation at high slice accelerations were also investigated from single-shot fMRI time series.

In the following theory section, we briefly review the blipped CAIPI technique, which was described in detail previously (Setsompop et al., 2012).

2. THEORY

The time domain MB EPI signal (ignoring the relaxation effects) in the presence of off-resonance effects, $\Delta B(x,y,z_l)$, can be expressed as:

$$s(t_m,t_n)=\sum_{l=1}^{MB}\int_{-\Delta z_l/2}^{\Delta z_l/2}\int_x\int_y \rho(x,y,z_l)\mathrm{e}^{-i\gamma\Delta B(x,y,z_l)(TE+mt_{dwell}+nt_{esp})}e^{-i\gamma(mG_xt_{dwell}x+nG_yt_{esp}y)}dxdydz_l \quad [1]$$

where MB is the number of simultaneously acquired slices, Δz is the slice thickness, $\rho(x,y,z_l)$ is the spin density modulated by transmit and receive variations, γ is the gyromagnetic ratio of the nucleus of interest, t_{esp} is the echo spacing, and t_{dwell} is the readout dwell time ($1/t_{dwell}$ is the readout bandwidth), m and n are *k*-space step indices

along the readout and phase encoding directions, G_x and G_y are idealized rectangular gradient amplitudes.

In a traditional multi-slice CAIPIRINHA GRE implementation (Breuer et al., 2005), the shifting of adjacent slices in a simultaneously excited group of slices is achieved through progressive phase shifts in the excitation pulse for consecutive acquisitions of each *k*-space line. In an EPI sequence, the corresponding phase shift has to be introduced by a gradient moment. For a particular MB factor, a unit PE_{SHIFT} blip moment (A_{blip}) can be calculated as:

$$A_{blip}=(2\pi PE_{SHIFT})/(\gamma\Delta S) \quad [2]$$

where PE_{SHIFT} is the desired amount of spatial shift proportional to the phase encoding field of view (FOV_{PE} in mm), ΔS (mm) is the separation between slice bands, and A_{blip} is the required blip gradient moment. Note that the blip gradient moment is independent of magnetic field strength (B_0), and is inversely proportional to the gyromagnetic ratio (γ) and slice band distance (ΔS).

Applying this unit blip gradient moment, scaled to an integer blip train pattern ($F(n)$, where n represents PE steps) as in the blipped CAIPI method, generates the desired phase differences between simultaneously excited slices in an MB acquisition, hence the desired spatial shift along the PE axis in image space. The resulting shifts are governed by the Fourier shift theorem (Bracewell, 1999), e.g., a blip train pattern of [1–1] for PE_{SHIFT} = FOV/2, [1 –2 1] for PE_{SHIFT} = FOV/3, [11 –31] for PE_{SHIFT} = FOV/4, and so forth. The starting phase difference is not important, because of the cyclic nature of the phase encoding dimension in *k*-space. This implies that an arbitrary pre-blip can be applied at the beginning of the EPI echo train.

As a result of the slice blip, for each *k*-space line there is an accumulated slice gradient blip moment, $A_{blip}^{Acum}(n)$, which is equal to the total area of the slice gradient blip (including any slice pre-blip, $A_{preblip}$) from the beginning of the EPI echo train:

$$A_{blip}^{Acum}(n)=\sum_{p=-k_y^{max}}^{n} F(p)A_{blip}(p)+A_{preblip} \quad [3]$$

where k_y^{max} is the largest phase encoding index. Hence, the MB EPI signal with blipped controlled aliasing can be expressed as:

$$s(t_m,t_n)=\sum_{l=1}^{MB}\int_{-\Delta z_l/2}^{\Delta z_l/2}\int_x\int_y \rho(x,y,z_l)\mathrm{e}^{(-i\gamma A_{blip}^{Acum}(n)z_l)}e^{-i\gamma\Delta B(x,y,z_l)(TE+mt_{dwell}+nt_{esp})}e^{-i\gamma(mG_xt_{dwell}x+nG_yt_{esp}y)}dxdydz_l \quad [4]$$

after slice off-center phases (a known quantity) have been subtracted.

In the blipped CAIPI method, a balancing pre-blip was chosen to minimize ghosting artifact in the point spread function (PSF) of the attenuated EPI echo train. As a result, slice gradient moment in units of half A_{blip} is always present for even PE_{SHIFT} factors for all *k*-space lines, while the periodic fully refocused slice gradient is retained for odd PE_{SHIFT} factors. Assuming the slice dependent residual phase error $\theta_1^{undesired}$ (with implicit in-plane terms),

$$\theta_l^{undesired}(t_m,t_n)=\int_{-\Delta z_l/2}^{\Delta z_l/2}\rho(\mathrm{z_l})e^{-i\gamma(A_{blip}^{Acum}(n)z_l+\Delta B(z_l)(TE+mt_{dwell}+nt_{esp}))}dz_l \quad [5]$$

is small compared to the desired blipped CAIPI phase modulation, the MB data can be satisfactorily unaliased using the slice-GRAPPA algorithm (Setsompop et al., 2012).

3. METHODS

3.1 Image acquisition

All in vivo experiments were performed on the 3 Tesla WU-Minn Human Connectome Project (Van Essen et al., 2012) Skyra scanner (Siemens, Erlangen, Germany) equipped with SC72 gradients operating at 100 mT/m maximum absolute gradient amplitude (maximum readout gradient amplitude, readout G_{max}, restricted to 42 mT/m for oblique slice orientations) with a maximum slew rate of 200 mT/m/ms (Heberlein et al., 2012; Kimmlingen et al., 2012). Imaging data were acquired with a standard 32-channel head receiver coil (Siemens) and a body transmitter. All data were obtained using a transverse oblique plane to cover the whole brain (about 12 – 13 cm of coverage in the slice dimension). A blipped CAIPI multiband EPI sequence (Appendix I) was used for all acquisitions.

Four healthy volunteers participated in this study. Two volunteers were scanned for slice unaliasing evaluation. We acquired single-shot fMRI time series on two other volunteers. Each participant provided written informed consent to the imaging protocol, which was approved by the institutional review board (IRB) at the University of Minnesota.

3.1.1 Slice unaliasing evaluation—The entire brain was covered using 60 or 64 slices and 2 mm isotropic resolutions with the following parameters: FOV = 192 × 192 mm^2, matrix = 96 × 96, partial Fourier = 6/8, TE/TR = 30/4800 ms, bandwidth = 2368 Hz/pixel, echo spacing = 0.55 ms, flip angle = 55° (<< Ernst angle ~ 90°, due to peak power limitation for MB = 12), sinc excitation pulse width = 12.8 ms, and no in-plane acceleration. Note that the excitation pulse width was not optimal for low MB factors. Instead, it was chosen in order to match the pulse width of the MB = 12 excitation pulse, which was limited by peak power despite the already reduced flip angle. Different multiband factors MB = 1, 2, 4, 6, 8, 10, and 12 were employed with the same PE_{SHIFT} = FOV/4, chosen for optimal slice unaliasing performance at very high slice acceleration factor (MB >= 8, see *L*-factor results below in Table 1 – 3). One single band (SB) reference scan was acquired before each MB acquisition for all MB acquisitions in this study. One hundred repetitions and five noise scans without excitation pulses were acquired for MB = 1 (i.e., SB), for the simulation of *g*-factors and signal leakage (*L*-) factors. Raw *k*-space data were used for evaluation as described in sections 3.2.4 and 3.2.5 below.

3.1.2 Single-shot fMRI time series—To assess the effect of increasing MB factor on the sampled physiological noise distribution, a set of resting state single-shot fMRI data was acquired (MB factors = 1, 3, 5, 7 and 9, FOV = 192 × 192 mm^2, matrix = 96 × 96, slice thickness 2 mm, partial Fourier = 7/8, TE/TR = 30/75 ms, bandwidth = 2368 Hz/pixel, echo spacing = 0.55 ms, flip angle = 20° (~ Ernst angle), sinc excitation pulse width = 6 ms, no in-plane acceleration, and 4096 measurements (approximately 5 minutes total acquisition time for each MB factor) from a healthy volunteer with simultaneous cardiac and respiratory monitoring at 400 Hz using a finger pulse oximeter (Siemens) and a chest breathing belt (Siemens). The TR (75ms) was minimized and matched across different MB factors. These were not whole brain acquisitions.

A *fixed volume* acquisition scheme was used in one volunteer. In MB = 1, only one slice at the center of the brain was acquired repeatedly at the rate of 75 ms per image. Similarly using the same 75 ms TR for MB = 3, 5, 7 and 9, multiband sequences simultaneously acquired 3, 5, 7, and 9 slices, respectively, using adequate slice distances (ΔS = 64 mm, 32

mm, 21.3 mm, and 16 mm, respectively) in a fixed volume to mimic realistic situations of whole brain coverage with MB = 2, 4, 6 and 8. The choice of odd MB factors in this experiment was for the convenience of slice co-localization with the MB = 1 acquisition during slice positioning. The slices were set so that one of the slices in MB > 1 acquisitions corresponded exactly (in ideal situation without subject motion) to the slice acquired in MB = 1. For MB = 3 and 5 acquisitions, a PE_{SHIFT} = FOV/3 was used, while for MB = 7 and 9, a PE_{SHIFT} = FOV/4 was used based on *L*-factor results (see Table 1 – 3) for optimal slice unaliasing.

In addition, a *fixed spacing* acquisition scheme was used for another volunteer in order to match multiple slice locations across different MB factors. The fixed slice spacing (ΔS) was chosen to be 21.3 mm, resulting in adequate whole brain coverage at MB = 7, nevertheless, under coverage for MB = 3 and 5 and over coverage for MB = 9. Two MB = 3 datasets were acquired with ΔS = 21.3 and 42.6 mm, respectively, resulting in five matched slice locations for MB = 3 with higher MB factor acquisitions. All other acquisition details were the same as in the fixed volume acquisition scheme.

A field map (2D gradient echo with FOV = 220 × 188 mm, matrix = 110 × 94, slice thickness = 2 mm, $TE_1/TE_2/TR$ = 4.92/7.38/650 ms, flip angle = 50°) was acquired in this experiment for routine geometric distortion correction.

3.2 Image reconstruction and evaluation

3.2.1 Slice unaliasing—In (Moeller et al., 2010), a slice-unaliasing algorithm was introduced based on a conventional GRAPPA algorithm. The GRAPPA kernel was calculated from a synthetic extended FOV (Blaimer et al., 2006). In (Setsompop et al., 2012), it was shown that this approach was not compatible with slice shifted acquisitions because of phase discontinuities. A slice-GRAPPA technique was proposed as a solution. The slice-GRAPPA multiband unaliasing implemented in this study was the same as in (Setsompop et al., 2012).

3.2.2 Image reconstruction pipeline and implementation—The slice-GRAPPA algorithm was implemented online on the scanner to output magnitude images in the same fashion as standard clinical images for the spectral analyses of the single-shot fMRI. The online reconstruction incorporated corrections for EPI image intensity variation and spatial shifts due to B_0 off-resonance modulations, for example, as induced by respiration (Pfeuffer et al., 2002), before the slice-GRAPPA operation. The partial *k*-space was zero-filled after the slice-GRAPPA operation.

3.2.3 Noise de-correlation—For unaliasing of signal with in-plane GRAPPA, it was shown in Breuer et al. (Breuer et al., 2009) that the noise-covariance is altered. Since the slice-GRAPPA algorithm is similar to the GRAPPA algorithm the noise-covariance of the signal between the different channels is also altered with the slice-GRAPPA algorithm. One way to represent the effect of this is to calculate a new slice-specific noise-correlation after noise has been unaliased with the slice-GRAPPA algorithm. For calculation of the new noise-covariance, N channels with noise were reconstructed with the slice-GRAPPA algorithm, followed by the calculation of the covariance between the noise-signals. After unaliasing of the N channels representing a multi-slice noise, each slice will have a signal in N channels representing slice-specific noise. The correlation of these signals can be used to estimate the noise-correlation. For a system with N channels and M simultaneously acquired slices, the N acquired signals were split into $N \times M$ signals with the slice-GRAPPA unaliasing algorithm. From the $N \times M$ noise signals, an $[N \times M] \times [N \times M]$ covariance matrix was calculated. Each $N \times N$ diagonal block was a measure of the slice-dependent

coil-correlation $\sigma^2(n_k^{unaliased})$ and was used for noise de-correlation from the multiple channels. Note that in the online reconstruction, the vendor implemented a spatially invariant noise de-correlation matrix [$N \times N$] estimated from a few *k*-space noise samples (by opening ADC in the absence of any RF or gradients) instead of from all slices in the image volume. In addition, the noise decorrelation is applied before the slice-GRAPPA algorithm. Despite these differences, we do not expect significant impact to the conclusions drawn in this paper for any adequately decoupled coil array.

3.2.4 Noise-amplification (*g*-factor)—For assessment of the noise-amplification (*g*-factor) with the slice-GRAPPA algorithm, the pseudo-replica method developed for both GRAPPA and non-Cartesian parallel imaging was used (Robson et al., 2008). Noise correlation and thermal noise level were estimated from a noise-only acquisition as described in section 3.2.3 above. With the known Gaussian noise level, a *k*-space representing pure thermal noise can be generated by drawing samples from a Gaussian distribution with the estimated noise level. A series of 100 repetitions of the same type of noise (each repetition having the same number of samples as what was acquired in *k*-space), with matched correlation and noise level, was generated for each channel. The noise was added to a single MB *k*-space (acquired without any repetitions) to generate a pseudo time series of the same image with 100 different noise images, and the 100 multiband *k*-spaces were un-aliased separately with the slice-GRAPPA algorithm. For each repetition of unaliased *k*-spaces with added noise, a combined image was constructed for each repetition and slice with a SENSE (R=1) algorithm (Lenglet et al., 2012; Sotiropoulos et al., 2013), which is the complex-valued, sensitivity-weighted, SNR-optimal combination for an array of correlated receivers (Roemer et al., 1990). The standard deviation of the real part of this signal, after it had been processed through the slice-GRAPPA algorithm, was compared with the real part of the noise signal itself. The ratio of the two defines the pixel specific noise amplification. A mask was defined for all signal inside the object based on a simple intensity threshold. Mean *g*-factors were calculated by averaging the values from all pixels within the mask. For evaluation of the range and distribution of *g*-factor values, histograms of all pixels in the mask were used.

3.2.5 Signal leakage (*L*-) factor due to residual aliasing—The *g*-factor as described in section 3.2.4 quantifies how much the SNR is reduced. More importantly, the multi-slice separation algorithm results in residual aliasing or signal leakage across simultaneously acquired slices. For signals from within the same slice, but from different channels, alterations to noise-correlations are not detrimental. However, correlations between signals originating from different slices are detrimental and will appear as residual aliasing or signal leakage. To evaluate signal leakage, the changes in the signal need to be quantified. This can only be achieved if the signal changes are known a priori. As such, a MB time series with 100 frames was formed such that

$$\mathrm{MB}(k,t)=\sum_{slices}\alpha(slice,t)\mathrm{SB}_{slice}(k) \quad [5]$$

where $\alpha(slice, t) = (1 + 0.1 \cdot \cos(4\pi \cdot slice \cdot t))$, $t = 0\ldots99$ and $slice = 1\ldots N$, and the SB's were single band acquisitions which had slice-specific phase shifts added to emulate any accumulated phase from gradient blipping. The choice of $\alpha(slice, t)$ was made such that the Fourier transform with respect to t of $\alpha(slice, t)$, $F(\alpha(slice, t))$ had a narrow linewidth limited by the number of points in the time-series. Let f_{slice} denote the values for each slice where $F(\alpha(slice, t))$ has its maximum. With the choices of imposed signal modulations for each slice $\alpha(slice, t)$, signals originating from a given aliased slice were well defined in the spectral frequency. From the synthesized MB time series, signal leaking from a given slice was

determined from $S_{slice}^{recon}(x,f)\text{for}f \neq \{f_{slice}\}$ by comparing those frequencies to $S_{slice}^{recon}(x,f)\text{for}f=\{f_{slice}\}$

To obtain comparable coefficients for calculating the amount of signal leakage, $S_{slice}^{recon}(x,f)$ was normalized for each f_{slice} such that $\sum_x |S_{slice}^{recon}(x,f_{slice})| \equiv 1$. To quantify the residual unaliased signal energy, $S_{slice'}^{recon}(x,f_{slice})$ was analyzed for signal when *slice'* ≠ *slice*. Signal leakage, referred to as the *L*-factor for each slice, is defined as $L-factor(slice',slice)=\mu(slice')\sum_x |S_{slice'}^{recon}(x,f_{slice})|$, masked to only include pixels in the brain (defined by a signal intensity threshold ε) and $\mu^{(-1)}(slice')=\sum_x \left(|S_{(slice')}^{recon}(x,0)|>\varepsilon\right)$. The *L*-factor has spatial variation, similar to the *g*-factor. To describe the spatial distribution of the *L*-factor for the whole imaging volume, three summary *L*-factor values are defined below.

A maximal *L*-factor $\max_{slice'\neq slice}\{\text{L}-\text{factor}(slice',slice)\}$ was calculated as the average slice specific maximal aliasing or signal leakage for the whole volume. Firstly, the *L*-factor was averaged within the mask for each slice; secondly, the slice (except the slice itself that was used to induce controlled signal fluctuations) with the maximal aliasing was identified among all slices and among all slice permutations for the induced controlled signal fluctuation within the MB slice group; and finally the maximal *L*-factor for each MB slice group was averaged among all MB slice groups to yield a single maximal *L*-factor value representing the entire acquisition volume.

Similarly a mean *L*-factor $\underset{slice'\neq slice}{\text{mean}}\{\text{L}-\text{factor}(slice',slice)\}$ was calculated as the average slice specific aliasing or signal leakage for the whole volume. The *L*-factor was first averaged within the mask for each slice as for the maximal *L*-factor. Then the mean *L*-factor was calculated by averaging over all slices (except the slice itself that was used to induce controlled signal fluctuations) and all slice permutations for the induced controlled signal fluctuation within the MB slice group, and all MB slice groups.

A ninety nine percentile (99%) *L*-factor was also calculated by first taking the 99% *L*-factor value within the mask for each slice. Then the 99% *L*-factor was averaged over all slices, permutations, and MB slice groups as described for the mean *L*-factor above.

3.3 Spectral analysis of single-shot fMRI time series

Image preprocessing was performed using (FSL 4.1.9, fsl.fmrib.ox.ac.uk). Each acquired slice in the single-shot fMRI datasets (2 mm isotropic and TR/TE = 75/30 ms) was 2D motion-corrected using the temporal mean volume as a reference (MCFLIRT, (Jenkinson et al., 2002)) and corrected for geometric distortion using the acquired field map (FUGUE, (Jenkinson et al., 2012; Jezzard and Balaban, 1995)), followed by time series linear detrending.

For the *fixed volume* data, spatial-temporal multi-taper filtering (Mitra et al., 1997; Percival and Walden, 1993) with singular value decomposition (SVD), was applied for energy partitioning for the formation of an aggregate coherence spectrum. In this method, the time-series datasets were first projected down from a center frequency to a frequency interval at direct current (DC) prior to performing SVD. The coherence was then assessed for each center frequency as the percentage of the energy that was captured by the dominant singular value. The process was repeated at each frequency in 0.01 Hz increment across the full spectral range up to the Nyquist limit (Mitra and Pesaran, 1999). Example coherence color maps at respiratory (0.3 Hz) and cardiac (1.2 Hz) frequencies were generated for the slice

that was common to all acquisitions, in order to compare spatial coherence patterns across increasing MB factors.

For the *fixed spacing* data, conventional power spectral densities (PSDs) were calculated as an alternative simpler way to assess the effect of increasing MB factor on sampled physiological noise distribution. PSDs were derived for each voxel time-course by averaging a set of independent spectral estimates obtained by using a multi-taper method (MTM), which employs a series of orthogonal Slepian sequences that are applied as data tapers prior to discrete Fourier transform (Mitra and Pesaran, 1999). PSD maps were then generated for spectral peaks at physiologic frequencies (e.g. cardiac and respiration along with their harmonics and interactions) by threshold relative to the standard deviation of the power densities over all voxels at the spectral peak frequency. Slices from two different fixed spacings for MB = 3 acquisitions were displayed together; while for MB = 7 and MB = 9 acquisitions the slices outside the central five slices were not shown.

4. RESULTS

4.1 Slice unaliasing

Slice unaliasing performance for blipped CAIPI was evaluated with almost fully relaxed magnetization (i.e., long TR whole brain acquisition as described in section 3.1.1) for MB factors up to 12 using 2 mm isotropic resolutions. Three representative (top, middle, and lower brain) slices, not from the same MB slice group, are shown from a whole brain acquisition (Fig. 1, top panel). Apparent image artifacts are negligible up to MB = 6. Image blurring and residual aliasing start to become noticeable at MB = 8; nevertheless even MB = 12 images still show respectable image quality. The achievable TR for a 60 or 64 slice whole brain acquisition with 2 mm isotropic resolution for the different MB factors are given below the images for each MB factor. The three-plane view of an MB = 8 image acquired with minimum TR = 0.6 s (Fig. 1, bottom panel) shows the effects of contrast difference and SNR reductions with high slice accelerations.

4.2 Noise amplification (*g*-factor)

Histograms of the *g*-factor over the entire brain (Fig. 2) show distributions with higher peak values and widths for higher MB factors, demonstrating increased noise amplification. As expected, the mean *g*-factor also increases with higher MB factors (Fig. 2). Comprehensive *g*-factor calculations for different MB factors with different PE_{SHIFT} are tabulated in the supplementary data (insert Supplementary Table 1 here). Notably, *g*-factors below unity were observed, especially prominent for MB = 2, indicating certain noise cancellation in parallel imaging based on slice unaliasing. Such a decrease below unity in GRAPPA construction was previously noted (Polimeni et al., 2008; Setsompop et al., 2012).

4.3 Signal leakage (*L*-) factor

Residual aliasing due to signal leakage from a particular slice into all other slices acquired simultaneously for a given MB factor and PE_{SHIFT} can be evaluated with *L*-factor maps (Fig. 3). Images with MB of 3, 4, 8 and 12 are illustrated with different shifts in the phase encoding direction. In each set, the amplitude of the modulation in one of the slices (slices that appear predominantly in red in Fig. 3) and the leakage of this modulation to other slices are shown using a color scale. The top row illustrates MB = 3 with PE_{SHIFT} = FOV/3 (Fig. 3A) and no PE_{SHIFT} (Fig. 3B). There is no perceptible leakage from the center slice to the two adjacent slices at this relatively low MB factor with or without PE_{SHIFT}. Note that rigorous statistical analysis of resting state fMRI were performed previously at MB = 3 without PE_{SHIFT} (Feinberg et al., 2010) and also with a PE_{SHIFT} = FOV/3 (Smith et al., 2012) and we use these conditions as a conservative benchmark to evaluate acceptable

performance (i.e., noise amplification and residual aliasing) of higher MB factors in this paper.

For higher MB factors the PE_{SHIFT} becomes more important. For MB = 4, for example, a PE_{SHIFT} of FOV/4 (Fig. 3C) significantly reduces the cross talk among the slices compared to that without PE_{SHIFT} (Fig. 3D). With MB = 8 (Fig. 3E) and even more so with MB = 12 (Fig. 3F), there is leakage present even with PE_{SHIFT} = FOV/4. Tables 1 and 2 list quantitative estimates of the signal leakage shown in Figure 3, using calculated parameters of the mean and maximum *L*-factors (as described in section 3.2.5) for different MB factors (up to MB = 12 with different PE_{SHIFT}). Table 3 tabulates ninety nine percentile *L*-factors. In these tables ΔS (mm) is the distance between simultaneously excited slices for a given MB factor with whole brain coverage.

4.4 Single-shot fMRI time series

It is well recognized that temporal fluctuations in an fMRI time series contain contributions from physiological processes such as cardiac pulsation and respiration and that these contributions affect the contrast-to-noise ratio (CNR) of the fMRI maps. Therefore, the temporal stability of the MB acquisition and the relative sensitivity to these physiological process were evaluated using time-series data obtained either with a single slice acquisition (i.e., MB = 1), or with multiband acquisitions using MB factors of 3, 5, 7 and 9, at the fastest TR achievable (75 ms, section 3.1.2) with 2 mm isotropic resolutions and TE = 30 ms. Within this TR, the number of slices acquired was equal to the MB factor.

In the *fixed volume* acquisition scheme, only one slice was common to all acquisitions. Coherence spectra were examined for this slice and are shown in Figure 4 for one subject. For comparison, power spectra are displayed for the simultaneously but separately acquired data from physiological monitoring devices (Fig. 4, bottom panel). Only the physiological data obtained during the MB = 9 acquisition are shown; others were similar. The spatial coherence maps (in color) for respiratory (0.3 Hz) and cardiac (1.2 Hz) frequencies superimposed on the anatomical image of the common center slice are illustrated next to the coherence spectra in Figure 4. These maps display the expected strongest coherences in the ventricles and at the edge of the brain due to respiration induced head movement and/or cerebrospinal fluid (CSF) pulsation. These maps resemble the commonly observed artifactual components from the spatial independent component analysis (ICA) of typical fMRI time series. The overall spatial patterns are consistent among different MB factors, despite the expected slightly more false positives and noisier coherence maps for MB > 5.

For the *fixed spacing* acquisition scheme, PSD maps for the five common slices in different MB factors show similar consistent spatial pattern for a cardiac modulated respiration peak at 1.05 Hz (insert Supplementary Figure 1 here).

5. DISCUSSION

The *g*-factor has been widely accepted as the *de-facto* metric for noise behavior in parallel imaging experiments. However, in fMRI, the more relevant noise source originates from temporal fluctuations, which are often dominated by physiological processes and not necessarily the thermal noise in a single image, to which the *g*-factor contributes. Hence a greater potential confound is the cross-contamination artifact among the simultaneously excited and acquired slices. Such cross-contamination can lead to false “activation” in slices, as we investigated in a previous study (Moeller et al., 2010). We propose here a new metric, *L*-factor (section 3.2.5), by which this cross-contamination can be systematically evaluated in a fashion analogous to the *g*-factor. Similar to the *g*-factor, the *L*-factor has spatial

variation. The mean, maximal, or 99% *L*- factor as calculated in this paper is one among many alternative definitions to summarize the *L*-factor distribution and variation.

The mean *L*-factor as defined in this manuscript may appear low in number despite the "total" amount of signal leakage can be substantial at high MB factors. However, we refrained from defining a "total" or combined leakage factor because the leakage signal can add either coherently or incoherently. The *L*-factors reported here represent the on average leakage from any given slice. The "total" mean or maximal leakage is not directly proportional to the reported on average *L*-factors or the MB factor.

If we take the performance of MB = 3 as an approximate guide, based on previous rigorous fMRI analyses of resting state fMRI time series (Feinberg et al., 2010; Smith et al., 2012) with some tolerance towards slightly higher *L*-factors, we can empirically consider a mean *L*-factor <= 0.05 and a maximum *L*-factor <= 0.9 acceptable. Caution should be noted, however, in that these *L*-factors, stated as "acceptable", are arbitrarily defined as an upper limit based on the integrity of previous fMRI experiments that demonstrated the expected spatial distributions and reliability in the functional maps. Additional rigorous fMRI analyses are needed to define more generalizable *L*-factor thresholds. Nevertheless, the observed leakage percentages, even at high MB factors remain comparable to typically observed in-plane EPI Nyquist ghosting levels, even at 7T (Poser et al., 2012; van der Zwaag et al., 2009). In addition, the *L*-factor could serve as a metric for evaluating different optimization strategies for the slice-GRAPPA kernel (Cauley et al., 2012; Setsompop and Wald, 2012).

Temporal stability of any acquisition method employed for fMRI is of critical importance since the functional CNR depends on the temporal fluctuations in an fMRI time series. Besides potential execution issues and various instrumental demands of a particular pulse sequence that can affect its temporal stability, how physiological noise sources arising from cardiac pulsation and respiration come into an acquisition scheme can be sequence dependent (e.g., see (Hu et al., 1995)). Therefore, the temporal stability of the MB technique was examined compared to that of a conventional single slice EPI acquisition in the fixed volume single-shot fMRI acquisition. The single-shot fMRI time series was employed to acquire images as fast as possible to minimize frequency aliasing in the spectral domain for a wide range of frequencies (TR = 75 ms). The MB approach was used to acquire 3, 5, 7 and 9 slices simultaneously at the same TR with one of the slices aligned to the slice employed in the single slice EPI acquisition. The choice of odd MB factors was for the convenience of the common center slice positioning. The two outermost slices defined the edge of the fixed volume, which needs one less MB factor than that in the single-shot fMRI dataset to cover in a multi-slice whole brain gapless acquisition. Hence our spectral results of MB = 3, 5, 7 and 9 in the fixed volume single-shot fMRI time series correspond to MB = 2, 4, 6 and 8 in practical whole brain fMRI acquisitions.

The analysis using spatio-temporal multi-taper analysis techniques ((Mitra et al., 1997), discussed further in the next paragraph) revealed similar components in the different MB time series although the spatial extend of the coherence at the cardiac frequency tended to increase somewhat for MB > 5, which we speculate to be due to increased residual aliasing and/or spatial blurring for higher MB factor images. The consistent correspondence of the various frequency components between MB = 1 and MB > 1 offers reassuring evidence that high MB factors (albeit with associated *g*-factor and *L*-factor penalties) do not necessarily obscure the neuronal activity of interest at low frequency or perturb signal fluctuations from physiological (i.e., cardiac or respiratory) sources.

The particular spectral analysis method used for the fixed volume single-shot fMRI acquisition is because of the spatio-temporal nature of the imaging data. Spectral consistency between the datasets acquired with increasing MB factors were initially assessed by verifying the correspondence of noise content from the monitored physiologic data using an average of PSD estimates of individual time-series calculated using multi-taper methods (Percival and Walden, 1993). However, the averaging of spectra over all the voxels in a dataset to form an aggregate spectrum tends to suppress complex spectral structure, thus, spatio-temporal multi-taper analysis techniques (Mitra et al., 1997) were employed. Although a simple time-space SVD of datasets does partition the energy spatially, it does so in a manner that does not generally correspond to something biologically relevant. For example, the cardiac and respiratory signal energies, two dominant sources of physiologic noise which are well localized and coherent in frequency and space (Hu et al., 1995), may interfere via a single beat tone partition and thus not be partitioned separately. This is the motivation for using a space-frequency SVD for energy partitioning for the formation of an aggregate spectrum. The resultant coherence spectrum (Fig. 4, top five panels) retains more of the complex structure when compared to the average PSD (data not shown) against the structure manifest in the power spectra of the simultaneously recorded physiologic signals (Fig. 4, bottom panel).

A conventional power spectral analysis was used, as an alternative simpler spectral analysis method, for the fixed spacing single-shot fMRI acquisitions to provide additional evidence at multiple common slice positions (supplementary data Fig. 1). Despite the fact of non-practical whole brain acquisition protocols for certain MB factors (i.e., under coverage for MB = 3 and MB = 5 and over coverage for MB = 9) due to the requirement of slice co-localization, the consistent spatial patterns for physiological frequency at different MB factors complements and corroborates the results from the fixed volume single-shot fMRI data.

The performance of parallel imaging using receiver coil sensitivity profiles depends on magnetic field strength (Ohliger et al., 2003; Wiesinger et al., 2006, 2004), as well as the number of coil elements and their layout in the multi-channel array employed for signal detection. Typically required in-plane accelerations and transmitter peak power may, however, limit high slice acceleration factors at 7 Tesla. In principle, though, higher slice accelerations would be feasible with a larger number of coil elements (Wiggins et al., 2009), especially along the slice direction. Therefore, the MB results presented here are specific to the field strength (3 Tesla) and the specific head coil (Siemens 32-channel head array for a Skyra system) employed (Wiggins et al., 2006).

In-plane accelerations were not used in this study in order to evaluate the full potential of slice accelerations at 3T. To obtain optimal BOLD contrast at 3T (Gati et al., 1997) without in-plane accelerations, partial Fourier factor of 6/8 or 7/8 were needed in this study at 2 mm isotropic resolution with a matrix size of 96. The HCP SC72 gradient used in the study allows readout G_{max} of ~ 42 mT/m, which is much stronger than a typical 3T clinical scanner with readout G_{max} of ~ 24 mT/m. The higher readout G_{max} helps to reduce echo spacing at high resolution in the readout direction. Hence partial Fourier and/or a longer TE would be required on a typical 3T scanner to achieve 2 mm isotropic resolution, without in-plane accelerations, as in this study. In addition, spatial blurring as well as susceptibility dropout could result from partial Fourier factors. Consequently, the choice of an MB GRE-EPI whole brain fMRI protocol on a 3T scanner depends on the tolerance to these negative consequences, the desired spatial resolution and volume coverage, and the need for ultra-short TRs. Through our extensive pilot evaluation within the HCP, including additional testing at Oxford University using 32 channel head coils at 3T (Griffanti et al., 2013), when in-plane accelerations are deemed not needed, MB factors of up to 8 (PE_{SHIFT} = FOV/3 or

FOV/4) are acceptable and, if needed, could be used to achieve the maximum reduction in TR for fMRI studies.

Understandably, the combination of phase encoding under-sampling and slice acceleration limits the maximum achievable slice acceleration factor. The effect of in-plane acceleration can be intuitively thought as folding of the FOV_{PE}, hence increasing the slice aliasing energy and reducing the effectiveness of controlled aliasing between slices. There are ongoing efforts to evaluate and improve the performance of such a two axis acceleration (Moeller et al., 2010), which is imperative for 7 Tesla applications of MB-EPI.

It is expected that the optimal PE shift (i.e., minimal *L*-factors and *g*-factors) increases as MB factor increases, e.g., an optimal PE_{SHIFT} = FOV/3 for MB = 6 and an optimal PE_{SHIFT} = FOV/4 for MB = 10. However, at high MB factors, there is a trade-off between minimizing direct (no relative shift between distant slices) overlap of MB slices versus maximizing PE_{SHIFT} between adjacent MB slices. Other factors influencing the *L*-factors and *g*-factors, and hence the optimal PE_{SHIFT}, include the size of the field-of view in the phase encode direction (i.e., FOV_{PE}) and the distance, ΔS, between adjacent slice bands, in addition to the specific field strength and receiver coil array. It is worth noting that, for protocol optimizations, the absolute values of the *L*-factors and *g*-factors, which depend on many experimental factors, are not as generalizable as the trends of these two metrics, as presented in the tables in this paper.

Spin echo (SE) MB-EPI does not typically operate at high slice acceleration factors (MB >= 3) due to peak power and/or specific absorption rate (SAR) limitations, or because of T_1 saturation effects (Setsompop et al., 2012). Recently, however, power independent of number of slices (PINS) RF pulses (Norris et al., 2011) have been demonstrated in SE-MB-EPI BOLD studies (Koopmans et al., 2012) to alleviate RF power limitations. Periodic modulation RF strategies, such as PINS pulses, have an unlimited FOV in the slice direction, requiring a careful selection of slice orientation, which may not necessarily be optimal for slice accelerations. Alternative approaches include variable-rate selective excitation (VERSE) (Conolly et al., 1988; Setsompop et al., 2012), optimized phase offsets between bands (Goelman, 1997; Hennig, 1992; Wong, 2012; Yao, 1995), or time shifting between individual bands can be applied (Auerbach et al., 2013; Goelman, 1997; Yao, 1995) to reduce peak power.

The high temporal efficiency of MB EPI with blipped CAIPI can be exploited in several different ways. Certainly, the most straightforward application is to acquire a time series with a higher rate of sampling, which we have shown improves the statistical significance of resting state networks (RSNs) (Feinberg et al., 2010), or to enable novel analysis methods, as we recently demonstrated with the use of temporal ICA to define temporally-independent functional modes (TFMs) (Smith et al., 2012). Alternatively, fMRI time series with multiple TEs (Kundu et al., 2012; Peltier and Noll, 2002; Poser et al., 2006; Posse et al., 1999; Speck and Hennig, 1998) can be acquired with an entire volume acquired inside the TE loop (Xu et al., 2012a) instead of the TE loop inside of the slice loop (i.e., multi-echo) (Olafsson et al., 2012). Auditory fMRI studies could also benefit hugely by using MB acceleration to reduce scanner noise interaction by reducing the image acquisition time and trading that gain for a prolonged silent period (Schwarzbauer et al., 2006), while keeping the same TR. However, because of the slow hemodynamic response and lower dimensional statistical analysis methods (Feinberg et al., 2010), block-designed task fMRI studies may not significantly benefit from very high slice acceleration factors. In certain applications at 3T, the temporal efficiency of MB EPI can also be traded-in for higher spatial resolution when a longer EPI echo train is not the limiting factor. Lastly, the blipped CAIPI technique can be combined with simultaneous image refocused (SIR) scheme to further reduce the volume acquisition

time (Feinberg et al., 2010; Setsompop et al., 2012), albeit at the expense of lengthening the EPI echo train.

Despite the focus on fMRI, the high acquisition efficiency has benefits far beyond fMRI. Any 2D GRE-EPI based acquisition, such as dynamic susceptibility contrast (DSC) imaging, arterial spin labeling (ASL), T_2* mapping, phase contrast velocity imaging (Fienberg et al., 2012), etc., could be significantly improved in temporal resolution when trade-off in lower image SNR (due to *g*-factor and T_1 saturation penalties) is affordable.

5. Conclusion

In this work, we demonstrated that multiband (MB) EPI, also known as simultaneous multi-slice (SMS) EPI, with the blipped CAIPI method can achieve high slice accelerations without significant degradations in image quality and without noise over-amplification or exaggerated residual aliasing. Our spectral analyses of single-shot fMRI verified that temporal fluctuations due to both neuronal and physiological sources are estimable, and could ultimately be removed through image analysis, even at very high slice acceleration factors. In the absence of in-plane accelerations, slice acceleration factors of up to 8 (MB = 8) can be routinely used in fMRI studies with a standard 32-channel head coil at 3 Tesla.

Supplementary Material

Refer to Web version on PubMed Central for supplementary material.

Acknowledgments

We appreciate the helpful discussions with Kawin Setsompop (Athinoula A. Martinos Center for Biomedical Imaging, Massachusetts General Hospital). We would also like to thank Dingxin Wang, Keith Heberlein, Thomas Benner, Michael Hamm, and Franz Schmitt (Siemens Healthcare Solutions) for their technical input to the Human Connectome Skyra scanner. This project was supported in part by the Human Connectome Project (U54MH091657-01) from the 16 National Institutes of Health (NIH) Institutes and Centers that support the NIH Blueprint for Neuroscience research, and by the National Center for Research Resources (P41 RR008079) and the National Institute of Biomedical Imaging and Bioengineering (P41 EB015894), as well as by NIH R44 NS073417, P30 NS057091 and P30 NS076408.

Appendix I: blipped CAIPI implementation

We used a pre-blip so as to assure, among the many refocusings and subsequent moment nullings for every FOV/PE_{SHIFT} phase encoding line, that the gradient moment at the *k*-space center line (k_0) was nulled (Xu et al., 2012b), thereby enforcing a fully refocused peak k_0 signal (insert Supplementary Figure 2 here). Our earlier implementation introduced an error from slice off-center phase inconsistencies between the SB reference and MB data, which resulted in degraded image quality for our implementation of the blipped CAIPI (Xu et al., 2012b, Fig. 3). With correct implementation, the standard blipped CAIPI sequence and the aligned version produce image reconstruction results that are not noticeably different for all MB acceleration factors reported in this work.

REFERENCES

Auerbach EJ, Xu J, Yacoub E, Moeller S, Uğurbil K. Multiband accelerated spinecho echo planar imaging with reduced peak RF power using time-shifted RF pulses. Magn. Reson. Med. 2013; 69:1261–1267. [PubMed: 23468087]

Banerjee, S.; Zur, Y.; Takahashi, A.; Shankaranarayan, A.; Kelley, DAC. Proc. Intl. Soc. Mag. Reson. Med. Melbourne, Australia: 2012. Time-Interleaved Parallel Imaging Approach to Separation of Simultaneously Excited Slices; p. 2227

Blaimer M, Breuer FA, Seiberlich N, Mueller MF, Heidemann RM, Jellus V, Wiggins G, Wald LL, Griswold MA, Jakob PM. Accelerated volumetric MRI with a SENSE/GRAPPA combination. J. Magn. Reson. Imaging. 2006; 24:444–450. [PubMed: 16786571]

Bracewell, R. The Fourier Transform & Its Applications. 3rd ed.. McGraw-Hill Science/Engineering/Math; 1999.

Breuer FA, Blaimer M, Heidemann RM, Mueller MF, Griswold MA, Jakob PM. Controlled aliasing in parallel imaging results in higher acceleration (CAIPIRINHA) for multi-slice imaging. Magn. Reson. Med. 2005; 53:684–691. [PubMed: 15723404]

Breuer FA, Kannengiesser SAR, Blaimer M, Seiberlich N, Jakob PM, Griswold MA. General formulation for quantitative G-factor calculation in GRAPPA reconstructions. Magn. Reson. Med. 2009; 62:739–746. [PubMed: 19585608]

Cauley, SF.; Setsompop, K.; Polimeni, JR.; Wald, LL. Proc. Intl. Soc. Mag. Reson. Med. Melbourne, Australia: 2012. Inter-slice artifact reduction for slice-GRAPPA reconstruction of simultaneous multi-slice (SMS) acquisitions; p. 2543

Chu, A.; Nielsen, J-F.; Noll, DC. Proc. Intl. Soc. Mag. Reson. Med. Melbourne, Australia: 2012. Increased Temporal Resolution in fMRI Using Hadamard-Encoding with Phase Correction and Physiological Noise Removal; p. 2858

Conolly S, Nishimura D, Macovski A, Glover G. Variable-rate selective excitation. J. Magn. Reson. 1969. 1988; 78:440–458.

De Martino F, Esposito F, van de Moortele P-F, Harel N, Formisano E, Goebel R, Ugurbil K, Yacoub E. Whole brain high-resolution functional imaging at ultra high magnetic fields: An application to the analysis of resting state networks. NeuroImage. 2011; 57:1031–1044. [PubMed: 21600293]

Feinberg DA, Hale JD, Watts JC, Kaufman L, Mark A. Halving MR imaging time by conjugation: demonstration at 3.5 kG. Radiology. 1986; 161:527–531. [PubMed: 3763926]

Feinberg DA, Moeller S, Smith SM, Auerbach E, Ramanna S, Glasser MF, Miller KL, Ugurbil K, Yacoub E. Multiplexed Echo Planar Imaging for Sub-Second Whole Brain FMRI and Fast Diffusion Imaging. Plos One. 2010; 5:e15710. [PubMed: 21187930]

Feinberg DA, Oshio K. Phase errors in multi shot echo planar imaging. Magn. Reson. Med. 1994; 32:535–539. [PubMed: 7997122]

Feinberg DA, Reese TG, Wedeen VJ. Simultaneous echo refocusing in EPI. Magn. Reson. Med. 2002; 48:1–5. [PubMed: 12111925]

Fienberg, D.; Chen, L.; Vu, A. Proc. Intl. Soc. Mag. Reson. Med. Melbourne, Australia: 2012. Multiband Velocity EPI; p. 2499

Frost, R.; Porter, DA.; Douaud, G.; Jezzard, P.; Miller, KL. Proc. Intl. Soc. Mag. Reson. Med. Melbourne, Australia: 2012. Reduction of Diffusion-Weighted Readout-Segmented EPI Scan Time Using a Blipped-CAIPI Modification; p. 116

Gati JS, Menon RS, Uğurbil K, Rutt BK. Experimental determination of the BOLD field strength dependence in vessels and tissue. Magn. Reson. Med. 1997; 38:296–302. [PubMed: 9256111]

Goelman G. Two methods for peak RF power minimization of multiple inversion-band pulses. Magn. Reson. Med. 1997; 37:658–665. [PubMed: 9126939]

Golay X, Pruessmann KP, Weiger M, Crelier GR, Folkers PJM, Kollias SS, Boesiger P. PRESTO SENSE: An ultrafast whole brain fMRI technique. Magn. Reson. Med. 2000; 43:779–786. [PubMed: 10861870]

Griffanti L, Salimi-Khorshidi G, Beckmann C, Auerbach E, Douaud G, Ebmeier K, Filippini N, Mackay C, Moeller S, Xu J, Yacoub E, Baselli G, Ugurbil K, Miller K, Smith S. Automated artefact removal and accelerated fMRI acquisition for improved Resting State Network imaging. Neuroimage. 2013

Griswold MA, Jakob PM, Heidemann RM, Nittka M, Jellus V, Wang J, Kiefer B, Haase A. Generalized autocalibrating partially parallel acquisitions (GRAPPA). Magn. Reson. Med. 2002; 47:1202–1210. [PubMed: 12111967]

Heberlein, K.; Kimmlingen, R.; Eberlein, E.; Hoecht, P.; Wang, D.; Witzel, T.; Tisdall, D.; Keil, B.; Adriany, G.; Auerbach, E.; Xu, J.; Yacoub, E.; Moeller, S.; Feinberg, D.; Wald, L.; Ugurbil, K.; Van Essen, D.; Wedeen, V.; Schmitt, F. Engineering the Human Connectome Project: concepts

and realization of high performace MR; Presented at the 18th Annual Meeting of the Organization for Human Brain Mapping; Beijing, China. 2012. p. 649

Heidemann RM, Ivanov D, Trampel R, Fasano F, Meyer H, Pfeuffer J, Turner R. Isotropic submillimeter fMRI in the human brain at 7 T: Combining reduced field-of-view imaging and partially parallel acquisitions. Magn. Reson. Med. 2012; 68:1506–1516. [PubMed: 22231859]

Hennig J. Chemical shift imaging with phase-encoding RF pulses. Magn. Reson. Med. 1992; 25:289–298. [PubMed: 1614312]

Hu X, Le TH, Parrish T, Erhard P. Retrospective estimation and correction of physiological fluctuation in functional MRI. Magn. Reson. Med. 1995; 34:201–212. [PubMed: 7476079]

Jenkinson M, Bannister P, Brady M, Smith S. Improved Optimization for the Robust and Accurate Linear Registration and Motion Correction of Brain Images. NeuroImage. 2002; 17:825–841. [PubMed: 12377157]

Jenkinson M, Beckmann CF, Behrens TEJ, Woolrich MW, Smith SM. FSL. NeuroImage. 2012; 62:782–790. [PubMed: 21979382]

Jesmanowicz A, Nencka AS, Li S-J, Hyde JS. Two-Axis Acceleration of Functional Connectivity Magnetic Resonance Imaging by Parallel Excitation of Phase-Tagged Slices and Half k-Space Acceleration. Brain Connect. 2011; 1:81–90. [PubMed: 22432957]

Jezzard P, Balaban RS. Correction for geometric distortion in echo planar images from B0 field variations. Magn. Reson. Med. 1995; 34:65–73. [PubMed: 7674900]

Kimmlingen, R.; Eberlein, E.; Dietz, P.; Kreher, S.; Schuster, J.; Riegler, J.; Matschl, V.; Schnetter, V.; Schmidt, A.; Lenz, H.; Mustaf, E.; Fischer, D.; Potthast, A.; Kreischer, L.; Eberler, M.; Hebrank, F.; Thein, H.; Heberlein, K.; Hoecht, P.; Witzel, T.; Tisdall, D.; Xu, J.; Yacoub, E.; Adriany, G.; Auerbach, E.; Moeller, S.; Feinberg, D.; Lehne, D.; Wald, L.; Fischl, B.; Ugurbil, K.; van Essen, D.; Wedeen, V.; Schmitt, F. Proc. Intl. Soc. Mag. Reson. Med. Melbourne, Australia: 2012. Concept and realization of high strength gradients for the Human Connectome Project; p. 696

Koopmans PJ, Boyacioğlu R, Barth M, Norris DG. Whole brain, high resolution spin-echo resting state fMRI using PINS multiplexing at 7 T. NeuroImage. 2012; 62:1939–1946. [PubMed: 22683385]

Kundu P, Inati SJ, Evans JW, Luh WM, Bandettini PA. Differentiating BOLD and non-BOLD signals in fMRI time series using multi-echo EPI. NeuroImage. 2012; 60:1759–1770. [PubMed: 22209809]

Larkman DJ, Hajnal JV, Herlihy AH, Coutts GA, Young IR, Ehnholm G. Use of multicoil arrays for separation of signal from multiple slices simultaneously excited. J. Magn. Reson. Imaging. 2001; 13:313–317. [PubMed: 11169840]

Lenglet, C.; Sotiropoulos, S.; Moeller, S.; Xu, J.; Auerback, E.; Yacoub, E.; Feinberg, D.; Setsompop, K.; Wald, L.; Behrens, T.; Ugurbil, K. Proc. Intl. Soc. Mag. Reson. Med. Melbourne, Australia: 2012. Multichannel diffusion MR image reconstruction: how to reduce elevated noise floor and improve fiber orientation estimation; p. 3538

Liu G, Sobering G, Duyn J, Moonen CTW. A. functional MRI technique combining principles of echo shifting with a train of observations (PRESTO). Magn. Reson. Med. 1993; 30:764–768. [PubMed: 8139461]

Loenneker T, Hennel F, Hennig J. Multislice interleaved excitation cycles (MUSIC): An efficient gradient-echo technique for functional MRI. Magn. Reson. Med. 1996; 35:870–874. [PubMed: 8744015]

Mansfield P. Multi-planar image formation using NMR spin echoes. J. Phys. C Solid State Phys. 1977; 10:L55–L58.

Mansfield P, Harvey PR, Stehling MK. Echo-volumar imaging. Magma Magn. Reson. Mater. Phys. Biol. Med. 1994; 2:291–294.

Mitra PP, Ogawa S, Hu X, Uğurbil K. The nature of spatiotemporal changes in cerebral hemodynamics as manifested in functional magnetic resonance imaging. Magn. Reson. Med. 1997; 37:511–518. [PubMed: 9094072]

Mitra PP, Pesaran B. Analysis of Dynamic Brain Imaging Data. Biophys. J. 1999; 76:691–708. [PubMed: 9929474]

Moeller, S.; Auerbach, E.; Van de Moortele, P-F.; Adriany, G.; Ugurbil, K. Proc. Intl. Soc. Mag. Reson. Med. Toronto, Ontario, Canada: 2008. fMRI with 16 fold reduction using multibanded multislice sampling; p. 2366

Moeller S, Van de Moortele P-F, Goerke U, Adriany G, Ugurbil K. Application of parallel imaging to fMRI at 7 Tesla utilizing a high 1D reduction factor. Magn. Reson. Med. Off. J. Soc. Magn. Reson. Med. Soc. Magn. Reson. Med. 2006; 56:118–129.

Moeller, S.; Xu, J.; Auerbach, EJ.; Yacoub, E.; Ugurbil, K. Proc. Intl. Soc. Mag. Reson. Med. Melbourne, Australia: 2012. Signal Leakage(L-Factor) as a Measure for Parallel Imaging Performance Among Simultaneously Multi-Slice (SMS) Excited and Acquired Signals, in; p. 519

Moeller S, Yacoub E, Olman CA, Auerbach E, Strupp J, Harel N, Uğurbil K. Multiband multislice GE-EPI at 7 tesla, with 16-fold acceleration using partial parallel imaging with application to high spatial and temporal whole-brain fMRI. Magn. Reson. Med. 2010; 63:1144–1153. [PubMed: 20432285]

Norris DG, Koopmans PJ, Boyacioğlu R, Barth M. Power independent of number of slices (PINS) radiofrequency pulses for low-power simultaneous multislice excitation. Magn. Reson. Med. 2011; 66:1234–1240. [PubMed: 22009706]

Nunes, RG.; Hajnal, JV.; Golay, X.; Larkman, DJ. Proc. Intl. Soc. Mag. Reson. Med. Seattle, Washington, USA: 2006. Simultaneous slice excitation and reconstruction for single shot EPI, in; p. 293

Ohliger MA, Grant AK, Sodickson DK. Ultimate intrinsic signal to noise ratio for parallel MRI: Electromagnetic field considerations. Magn. Reson. Med. 2003; 50:1018–1030. [PubMed: 14587013]

Olafsson, V.; Guo, J.; Wong, CW.; Kundu, P.; Inati, S.; Luh, W-M.; Roopchansingh, V.; Brenowitz, N.; Bandettini, P.; Wong, E.; Liu, T. Proc. Intl. Soc. Mag. Reson. Med. Melbourne, Australia: 2012. High spatial and temporal resolution fcMRI with BOLD selectivity using multiecho simultaneous multislice EPI; p. 2068

Peltier SJ, Noll DC. T2* Dependence of Low Frequency Functional Connectivity. NeuroImage. 2002; 16:985–992. [PubMed: 12202086]

Percival, DB.; Walden, AT. Spectral Analysis for Physical Applications. 1st ed.. Cambridge University Press; 1993.

Pfeuffer J, Van de Moortele P, Ugurbil K, Hu X, Glover GH. Correction of physiologically induced global off resonance effects in dynamic echo planar and spiral functional imaging. Magn. Reson. Med. 2002; 47:344–353. [PubMed: 11810679]

Polimeni JR, Fischl B, Greve DN, Wald LL. Laminar analysis of 7 T BOLD using an imposed spatial activation pattern in human V1. NeuroImage. 2010; 52:1334–1346. [PubMed: 20460157]

Polimeni, JR.; Setsompop, K.; Gagoski, BA.; McNab, JA.; Triantafyllou, C.; Wald, LL. Proc. Intl. Soc. Mag. Reson. Med. Melbourne, Australia: 2012. Rapid multi-shot segmented EPI using the Simultaneous Multi-Slice acquisition method; p. 2222

Polimeni, JR.; Wiggins, GC.; Wald, LL. Proc. Intl. Soc. Mag. Reson. Med. Toronto, Ontario, Canada: 2008. Characterization of artifacts and noise enhancement introduced by GRAPPA reconstructions; p. 1286

Poser BA, Barth M, Goa P-E, Deng W, Stenger VA. Single shot echo planar imaging with Nyquist ghost compensation: Interleaved dual echo with acceleration (IDEA) echo planar imaging (EPI). Magn. Reson. Med. 2012

Poser BA, Koopmans PJ, Witzel T, Wald LL, Barth M. Three dimensional echo- planar imaging at 7 Tesla. NeuroImage. 2010; 51:261–266. [PubMed: 20139009]

Poser, BA.; Stenger, VA. Proc. Intl. Soc. Mag. Reson. Med. Melbourne, Australia: 2012. Multiplexed spiral sequence for high temporal resolution resting state fMRI; p. 2857

Poser BA, Versluis MJ, Hoogduin JM, Norris DG. BOLD contrast sensitivity enhancement and artifact reduction with multiecho EPI: Parallel acquired inhomogeneity desensitized fMRI. Magn. Reson. Med. 2006; 55:1227–1235. [PubMed: 16680688]

Posse S, Ackley E, Mutihac R, Rick J, Shane M, Murray-Krezan C, Zaitsev M, Speck O. Enhancement of temporal resolution and BOLD sensitivity in real-time fMRI using multi-slab echo-volumar imaging. NeuroImage. 2012; 61:115–130. [PubMed: 22398395]

Posse S, Wiese S, Gembris D, Mathiak K, Kessler C, Grosse Ruyken M, Elghahwagi B, Richards T, Dager SR, Kiselev VG. Enhancement of BOLD contrast sensitivity by single shot multi echo functional MR imaging. Magn. Reson. Med. 1999; 42:87–97. [PubMed: 10398954]

Pruessmann KP, Weiger M, Scheidegger MB, Boesiger P. SENSE: Sensitivity encoding for fast MRI. Magn. Reson. Med. 1999; 42:952–962. [PubMed: 10542355]

Robson PM, Grant AK, Madhuranthakam AJ, Lattanzi R, Sodickson DK, McKenzie CA. Comprehensive quantification of signal to noise ratio and g factor for image based and k space based parallel imaging reconstructions. Magn. Reson. Med. 2008; 60:895–907. [PubMed: 18816810]

Roemer PB, Edelstein WA, Hayes CE, Souza SP, Mueller OM. The NMR phased array. Magn. Reson. Med. 1990; 16:192–225. [PubMed: 2266841]

Schwarzbauer C, Davis MH, Rodd JM, Johnsrude I. Interleaved silent steady state (ISSS) imaging: A new sparse imaging method applied to auditory fMRI. NeuroImage. 2006; 29:774–782. [PubMed: 16226896]

Setsompop K, Gagoski BA, Polimeni JR, Witzel T, Wedeen VJ, Wald LL. Blipped controlled aliasing in parallel imaging for simultaneous multislice echo planar imaging with reduced g factor penalty. Magn. Reson. Med. 2012; 67:1210–1224. [PubMed: 21858868]

Setsompop, K.; Wald, LL. Proc. Intl. Soc. Mag. Reson. Med. Melbourne, Australia: 2012. A Multi-Kernel Approach for Reducing Inter-Slice Image Ghosting in Simultaneous Multi-Slice EPI; p. 3349

Smith SM, Miller KL, Moeller S, Xu J, Auerbach EJ, Woolrich MW, Beckmann CF, Jenkinson M, Andersson J, Glasser MF, Van Essen DC, Feinberg DA, Yacoub ES, Ugurbil K. Temporally-independent functional modes of spontaneous brain activity. Proc. Natl. Acad. Sci. 2012

Sodickson DK, Manning WJ. Simultaneous acquisition of spatial harmonics (SMASH): Fast imaging with radiofrequency coil arrays. Magn. Reson. Med. 1997; 38:591–603. [PubMed: 9324327]

Sotiropoulos SN, Moeller S, Jbabdi S, Xu J, Andersson JL, Auerbach EJ, Yacoub E, Feinberg D, Setsompop K, Wald LL, Behrens TEJ, Ugurbil K, Lenglet C. Effects of image reconstruction on fibre orientation mapping from multichannel diffusion MRI: Reducing the noise floor using SENSE. Magn. Reson. Med. 2013 n/a–n/a.

Speck O, Hennig J. Functional Imaging by I0- and T2* -parameter mapping using multi-image EPI. Magn. Reson. Med. 1998; 40:243–248. [PubMed: 9702706]

Stäb D, Ritter CO, Breuer FA, Weng AM, Hahn D, Köstler H. CAIPIRINHA accelerated SSFP imaging. Magn. Reson. Med. 2011; 65:157–164. [PubMed: 20872868]

Uğurbil K. The road to functional imaging and ultrahigh fields. NeuroImage. 2012; 62:726–735. [PubMed: 22333670]

Van der Zwaag W, Marques JP, Lei H, Just N, Kober T, Gruetter R. Minimization of Nyquist ghosting for echo-planar imaging at ultra-high fields based on a “negative readout gradient” strategy. J. Magn. Reson. Imaging. 2009; 30:1171–1178. [PubMed: 19856451]

Van Essen DC, Ugurbil K, Auerbach E, Barch D, Behrens TEJ, Bucholz R, Chang A, Chen L, Corbetta M, Curtiss SW, Della Penna S, Feinberg D, Glasser MF, Harel N, Heath AC, Larson-Prior L, Marcus D, Michalareas G, Moeller S, Oostenveld R, Petersen SE, Prior F, Schlaggar BL, Smith SM, Snyder AZ, Xu J, Yacoub E. The Human Connectome Project: A data acquisition perspective. NeuroImage. 2012; 62:2222–2231. [PubMed: 22366334]

Wielopolski PA, Manning WJ, Edelman RR. Single breath hold volumetric imaging of the heart using magnetization prepared 3 dimensional segmented echo planar imaging. J. Magn. Reson. Imaging. 1995; 5:403–409. [PubMed: 7549201]

Wiesinger F, Van de Moortele P, Adriany G, De Zanche N, Ugurbil K, Pruessmann KP. Parallel imaging performance as a function of field strength—An experimental investigation using electrodynamic scaling. Magn. Reson. Med. 2004; 52:953–964. [PubMed: 15508167]

Wiesinger F, Van de Moortele P, Adriany G, De Zanche N, Ugurbil K, Pruessmann KP. Potential and feasibility of parallel MRI at high field. Nmr Biomed. 2006; 19:368–378. [PubMed: 16705638]

Wiggins GC, Polimeni JR, Potthast A, Schmitt M, Alagappan V, Wald LL. 96 Channel receive only head coil for 3 Tesla: Design optimization and evaluation. Magn. Reson. Med. 2009; 62:754–762. [PubMed: 19623621]

Wiggins GC, Triantafyllou C, Potthast A, Reykowski A, Nittka M, Wald LL. 32 channel 3 Tesla receive only phased array head coil with soccer ball element geometry. Magn. Reson. Med. 2006; 56:216–223. [PubMed: 16767762]

Wong, E. Proc. Intl. Soc. Mag. Reson. Med. Melbourne, Australia: 2012. Optimized Phase Schedules for Minimizing Peak RF Power in Simultaneous Multi-Slice RF Excitation Pulses; p. 2209

Xu, J.; Auerbach, E.; Moeller, S.; De Martino, F.; Feinberg, D.; Yacoub, E.; Ugurbil, K. Interleaved-TE fMRI acquisitions with highly accelerated multiband EPI; Beijing, China. Presented at the 18th Annual Meeting of the Organization for Human Brain Mapping; 2012a. p. 632

Xu, J.; Moeller, S.; Strupp, J.; Auerbach, E.; Chen, L.; Feinberg, D.; Ugurbil, K.; Yacoub, E. Proc. Intl. Soc. Mag. Reson. Med. Melbourne, Australia: 2012b. Highly accelerated whole brain imaging using aligned-blipped-controlled- aliasing multiband EPI; p. 2306

Yacoub E, Harel N, Uğurbil K. High-field fMRI unveils orientation columns in humans. Proc. Natl. Acad. Sci. 2008; 105:10607–10612. [PubMed: 18641121]

Yao C. Method and apparatus for substantially simultaneously exciting a plurality of slices in NMR imaging. 1995 5422572.

Yutzy SR, Seiberlich N, Duerk JL, Griswold MA. Improvements in multislice parallel imaging using radial CAIPIRINHA. Magn. Reson. Med. 2011; 65:1630–1637. [PubMed: 21287592]

Zimmermann J, Goebel R, De Martino F, van de Moortele P-F, Feinberg D, Adriany G, Chaimow D, Shmuel A, Uğurbil K, Yacoub E. Mapping the Organization of Axis of Motion Selective Features in Human Area MT Using High-Field fMRI. Plos One. 2011; 6:e28716. [PubMed: 22163328]

Highlights

- High slice accelerations using multiband (MB) GRE-EPI with blipped CAIPI.
- Acceptable MB factors up to 8 with a 32-channel receiver coil at 3T.
- Neuronal and physiological sources are distinguishable at high MB factors.
- Leakage (*L*-) factor evaluates residual aliasing among simultaneously acquired slices.
- High temporal efficiency with MB-EPI benefits various applications.

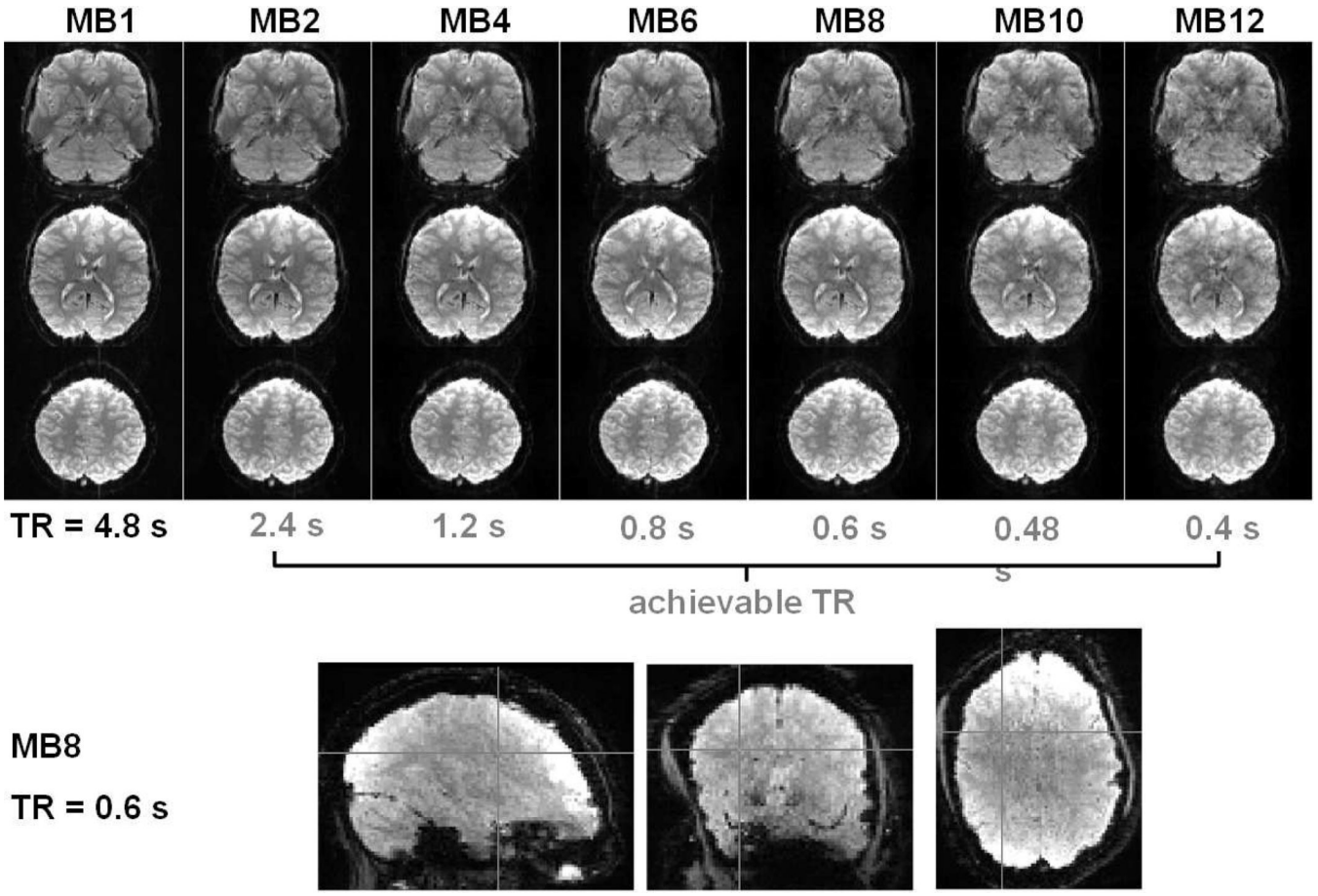

Figure 1.

Slice acceleration up to MB factor of 12 (upper panel) demonstrates negligible image degradation up to MB = 6 and good image quality up to MB = 8. Images were acquired with matched TR = 4.8 s at 2 mm isotropic resolution (60 or 64 slices) for comparison between MB factors. The example axial slices shown here were not from the same MB slice group. Achievable TR at a given MB factor is listed below the images to show the acceleration potential. Axial, coronal, and sagittal views of MB = 8 image from a different subject at minimum TR = 0.6 s (bottom panel) illustrate the contrast alteration and SNR compromises with TR reduction.

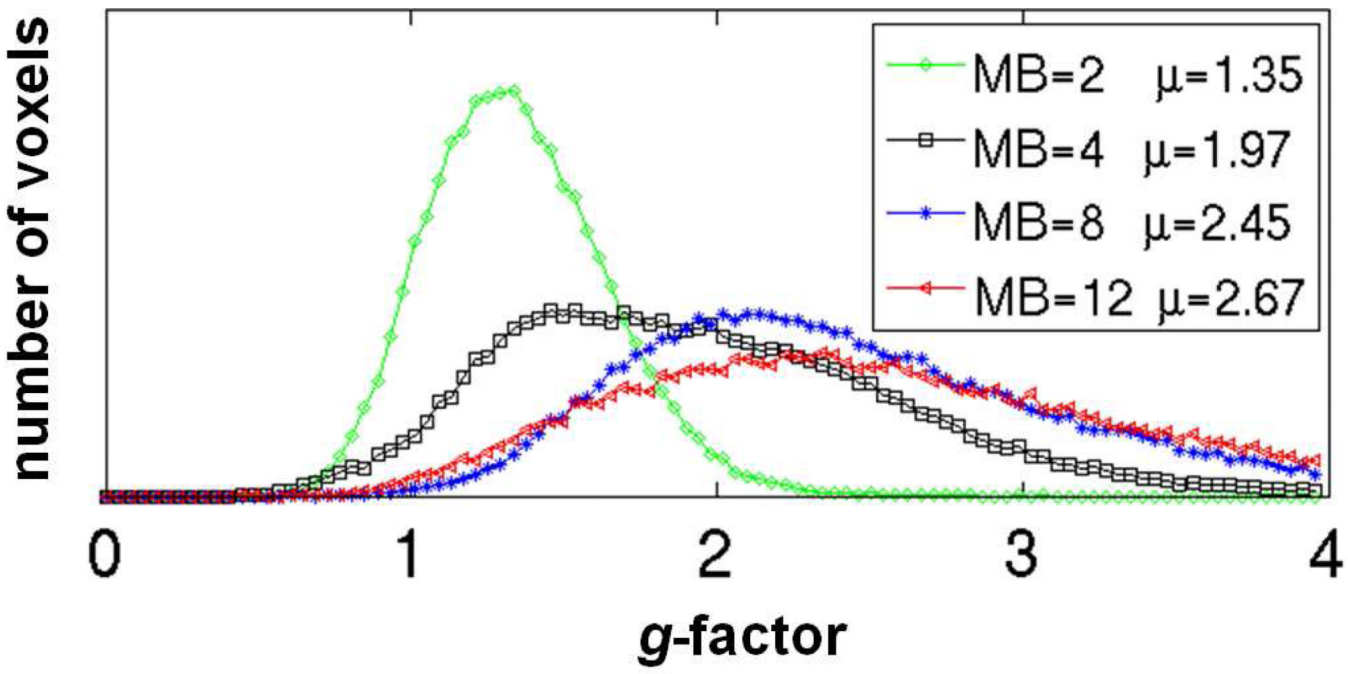

Figure 2.

Histograms of the *g*-factors over the entire brain show distributions with higher peak values and widths for higher MB factors, as well as the expected increase in mean *g*-factor (μ in the legend). Note that the noise standard deviation for the *g*-factor calculation was measured from the real part of the complex MR signal.

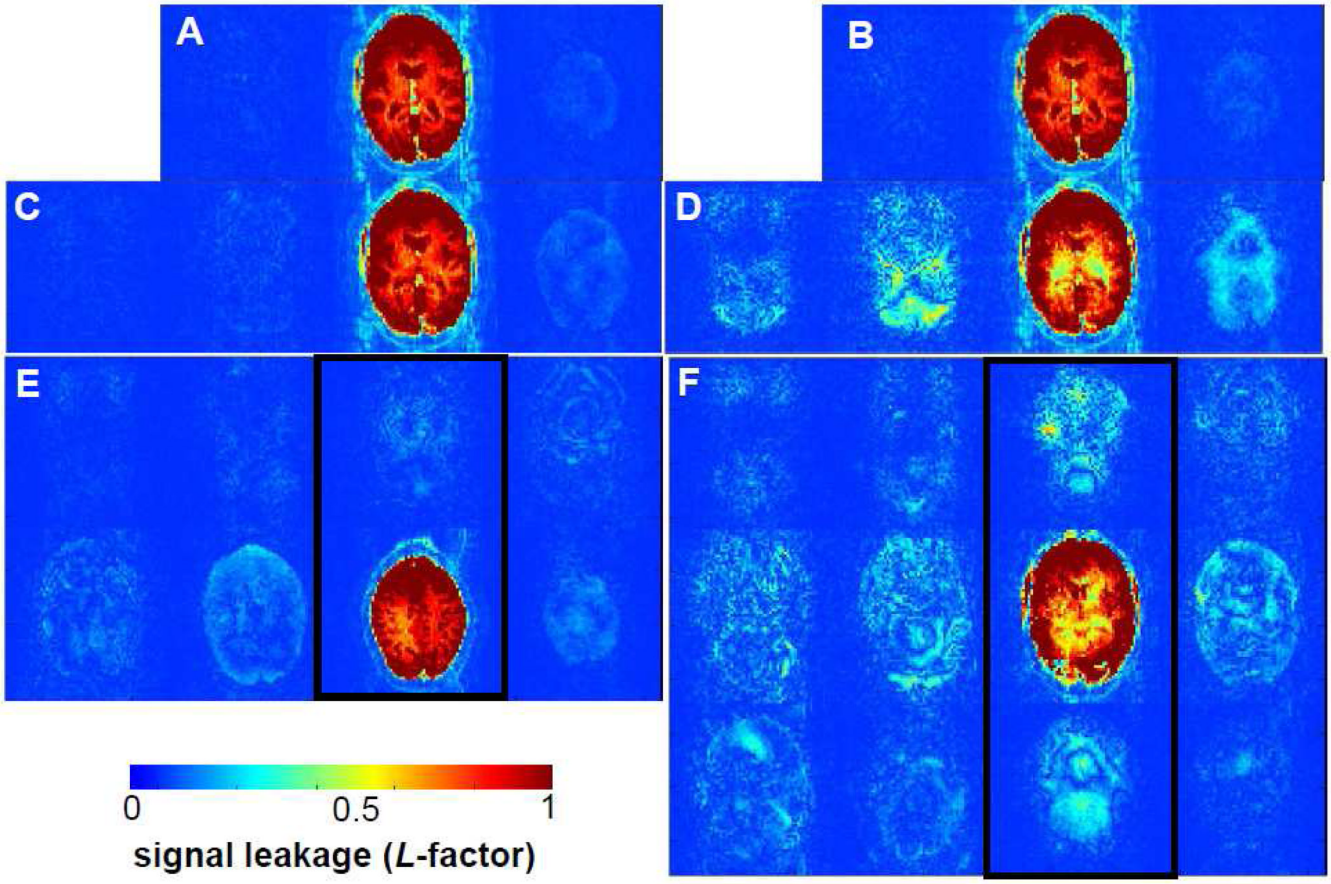

Figure 3.

Signal leakage (*L*-) factor maps show little difference in signal leakage for MB3 with PE_{SHIFT} = FOV/3 (A) or no PE_{SHIFT} (B), while there is significant difference in signal leakage for MB4 with PE_{SHIFT} = FOV/4 (C) and no PE_{SHIFT} (D). For high MB factors, e.g., MB = 8 (E) or MB = 12 (F), the signal leakage is most pronounced in adjacent simultaneously acquired slices, as well as those MB slices that directly overlap on top of each other (black boxes), despite the applied PE_{SHIFT} = FOV/4.

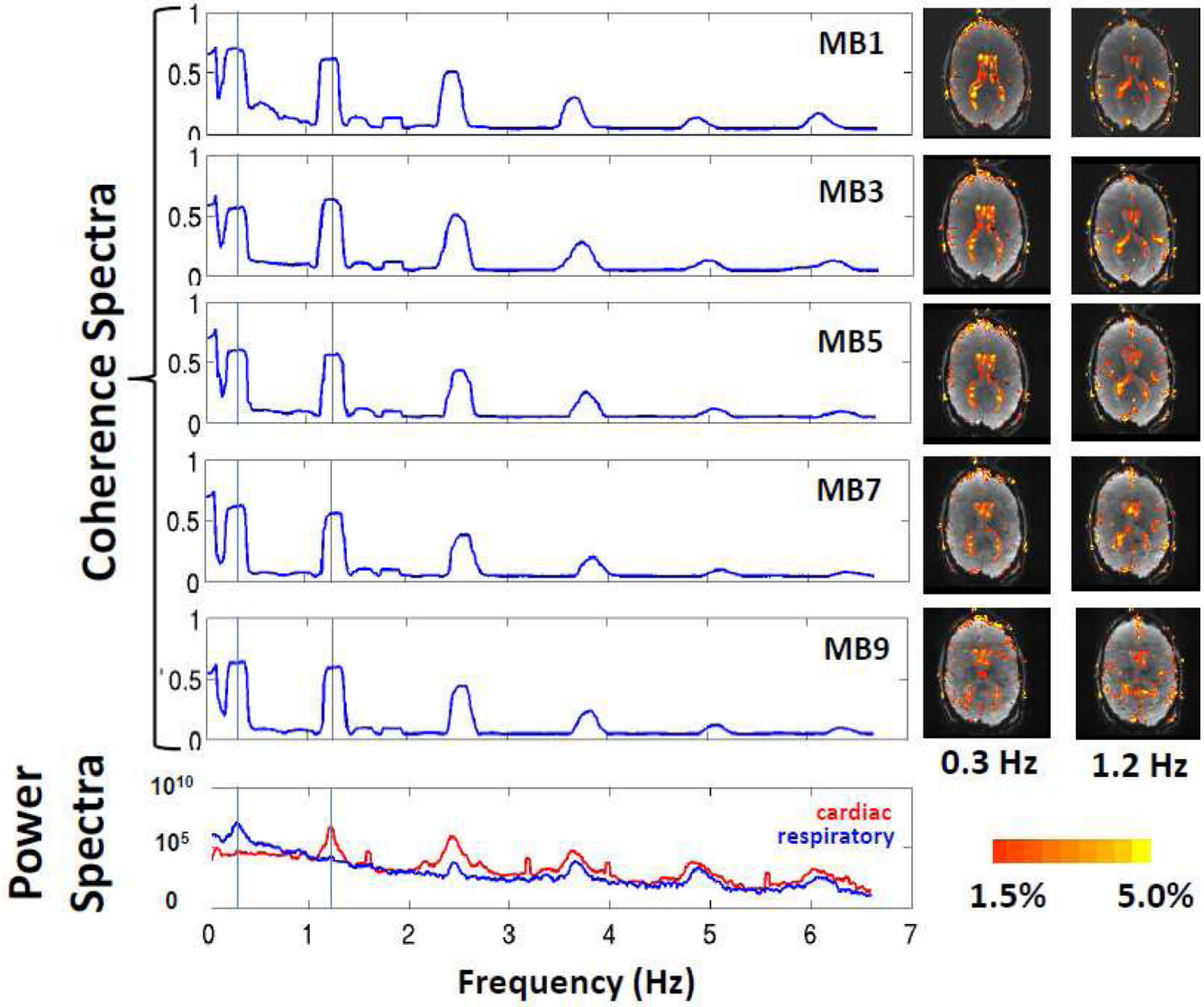

Figure 4.

Coherence spectra (top five panels) from fixed volume single-shot (TR/TE = 75/30 ms) resting state fMRI time series demonstrate consistent spectral components for different MB factors. Cardiac (bottom panel, red) and respiratory (bottom panel, blue) components from simultaneous physiological monitoring are co-localized in the frequency spectrum with those non-aliased spectral peaks in the coherence spectra. Spatial coherence maps (right of the coherence spectra) at respiratory (0.3 Hz) and cardiac (1.2 Hz) frequencies, showing the percentage of the energy captured by the dominant singular value, are overlaid on anatomical images for the center slice positioned in common during different MB acquisitions. The scale for the spatial coherence color maps (from 1.5% to 5.0%) is the coherence at the respiratory or cardiac frequency (same range for all MB factors).

Table 1

Mean signal leakage (*L*-) factor for different MB and PE_{SHIFT}. Reference mean *L*-factor (MB = 3, PE_{SHIFT} = 0, dark shaded cell) was based on previous experience (Feinberg et al., 2010). Unacceptable mean *L*-factors (> 0.05) are light shaded. ΔS (mm) is the distance between simultaneously excited slices for a given MB factor with whole brain coverage.

		MB=2 ΔS=64	MB=3 ΔS≈43	MB=4 ΔS=32	MB=6 ΔS=21	MB=8 ΔS=16	MB=10 ΔS≈13	MB=11 ΔS≈12	MB=12 ΔS≈11
PE_{SHIFT} (FOV)	0	.02	.03	.09	.17	.25	.26	.32	.30
	1/2	.02	.02	.02	.04	.09	.10	.14	.13
	1/3	.02	.02	.02	.02	.04	.05	.08	.07
	1/4	.02	.02	.02	.03	.03	.04	.05	.05
	1/5	.02	.02	.02	.03	.05	.05	.06	.05
	1/6	.02	.02	.03	.04	.06	.06	.07	.07

Table 2

Maximum signal leakage (*L*-) factor for different MB and PE_{SHIFT}. Reference maximum *L*-factor (MB = 3, PE_{SHIFT} = 0, dark shaded cell) was based on previous experience (Feinberg et al., 2010). Unacceptable maximum *L*-factors (> 0.9) are light shaded. ΔS (mm) is the distance between simultaneously excited slices for a given MB factor with whole brain coverage.

		MB=2 ΔS=64	MB=3 ΔS≈43	MB=4 ΔS=32	MB=6 ΔS=21	MB=8 ΔS=16	MB=10 ΔS≈13	MB=11 ΔS≈12	MB=12 ΔS≈11
PE_{SHIFT} (FOV)	0	.34	.44	1.2	2.4	4.6	5.5	6.9	6.9
	1/2	.23	.26	.33	.40	1.4	1.8	2.5	2.5
	1/3	.48	.29	.26	.26	.47	.77	1.4	1.4
	1/4	.32	.21	.33	.31	.44	.49	.72	.74
	1/5	.27	.25	.29	.41	.58	.67	.85	.81
	1/6	.26	.29	.41	.55	.97	1.0	1.1	1.1

Table 3

Ninety nine percentile (99%) sigal leakage (*L*-) factor for different MB and PE_{SHIFT}. Reference 99% *L*-factor (MB = 3, PE_{SHIFT} = 0, dark shaded cell) was based on previous experience (Feinberg et al., 2010). Unacceptable 99% *L*-factors (> 0.3) are light shaded. ΔS (mm) is the distance between simultaneously excited slices for a given MB factor with whole brain coverage.

		MB=2 AS=64	MB=3 AS«43	MB=4 AS=32	MB=6 AS=21	MB=8 AS=16	MB=10 AS«13	MB=11 AS«12	MB=12 AS«11
PE_{SHIFT} (FOV)	0	.08	.14	.40	.89	1.4	1.5	1.8	1.8
	1/2	.07	.07	.09	.16	.49	.64	.84	.80
	1/3	.07	.07	.08	.10	.17	.28	.46	.45
	1/4	.07	.07	.08	.11	.15	.18	.26	.26
	1/5	.07	.08	.09	.15	.22	.24	.29	.27
	1/6	.07	.08	.12	.20	.33	.34	.40	.37